

PAPER • OPEN ACCESS

Argon admixture-driven enhanced ionization and performance of a 5 kW Hall thruster on krypton

To cite this article: Dongho Lee *et al* 2024 *J. Phys. D: Appl. Phys.* **57** 325201

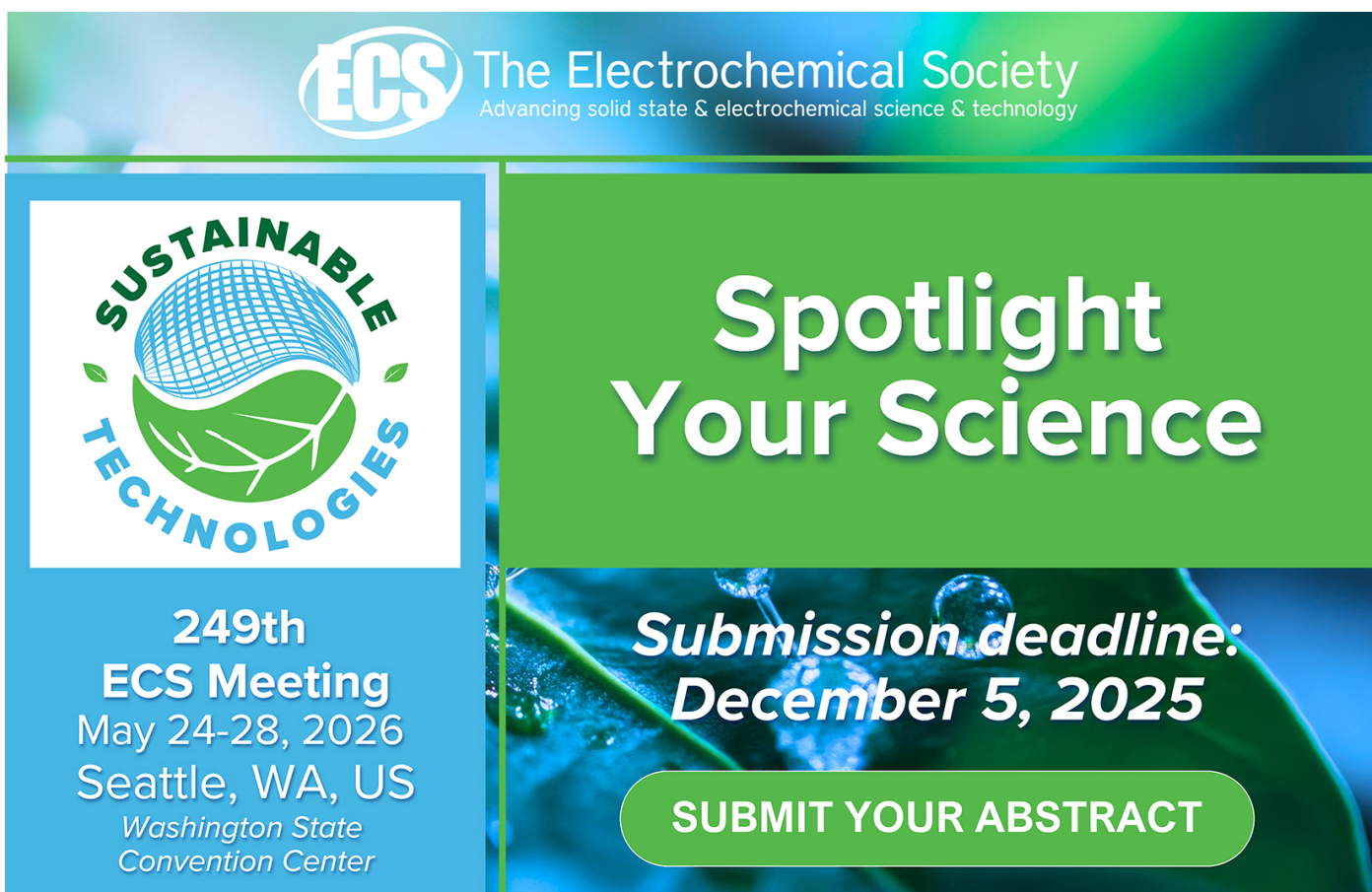
View the [article online](#) for updates and enhancements.

You may also like

- [The Abundances of Light Neutron-Capture Elements in Planetary Nebulae. I. Photoionization Modeling and Ionization Corrections](#)
N. C. Sterling, Harriet L. Dinerstein and T. R. Kallman

- [Quenching of the resonance \$5s\(^3P_1\)\$ state of the krypton atom in collisions with krypton and argon atoms](#)
D A Zayarnyi, A Yu L'dov and I V Kholin

- [Deactivation of krypton atoms in the metastable \$5s\(^3P_2\)\$ state in collisions with krypton and argon atoms](#)
D A Zayarnyi, A Yu L'dov and I V Kholin



The advertisement features the ECS logo and the text "The Electrochemical Society Advancing solid state & electrochemical science & technology". On the left, there's a circular logo for "SUSTAINABLE TECHNOLOGIES" with a stylized globe and leaves. Below it, the text reads: "249th ECS Meeting May 24-28, 2026 Seattle, WA, US Washington State Convention Center". On the right, the text "Spotlight Your Science" is displayed prominently in white, with a "Submission deadline: December 5, 2025" below it. A green button at the bottom right says "SUBMIT YOUR ABSTRACT".

Argon admixture-driven enhanced ionization and performance of a 5 kW Hall thruster on krypton

Dongho Lee*, William P Brabston, Dan Lev and Mitchell L R Walker

Daniel Guggenheim School of Aerospace Engineering, Georgia Institute of Technology, Atlanta, GA 30332, United States of America

E-mail: dlee968@gatech.edu

Received 2 November 2023, revised 30 March 2024

Accepted for publication 30 April 2024

Published 16 May 2024



Abstract

Utilizing alternative propellants has been recognized as a strategy to reduce the total cost of propellants in electric propulsion-based missions. The aim of this study is to quantify the Hall effect thruster (HET) performance and operating characteristics using a Kr–Ar mixture to enable mission designers to evaluate the impact on mission and spacecraft design. We present the performance and plume plasma properties of the P5 5 kW-class HET operated with a Kr–Ar mixture with Ar volumetric flow rate fractions from 0 to 100%. The thruster is characterized at discharge power levels of 2.6 kW and 4.1 kW at constant discharge current and voltage over the range of Ar fractions. Despite higher ionization energy and lower mass of Ar, the thruster exhibited a similar level of thrust within 2% when comparing the pure Kr and 26%-Ar mixture cases. The derived ion energy distribution functions and analytical modeling suggest that the characteristic length for the ionization region is extended as the Ar fraction increases. The increased residence time of Kr at the extended ionization region and background energetic electrons from the ionized Ar neutrals are considered to cause this enhanced ionization of the injected Kr neutrals. This leads to a 6% higher Kr ion density at the 26%-Ar case even at the 16% less injected Kr neutral density than in the pure Kr case. The enhanced Kr ionization and generated Ar ions in the 26%-Ar case consequently led to a comparable thrust with that of the pure Kr case. The study indicates that mixing Ar with approximately 26% volumetrically with Kr can provide a similar or even higher thrust performance at the same discharge power. This will be particularly advantageous for various space missions that require high impulses by reducing the total cost of the propellant.

Keywords: Hall thruster plasmas, alternative propellants, Kr–Ar mixture, ionization region

1. Introduction

Hall effect thrusters (HETs) are extensively utilized electric propulsion devices that generate thrust by accelerating ions

using electric fields [1–4]. The neutral particles are injected into an annular discharge channel and then ionized by electrons that exhibit $E \times B$ drift motions by axial electric and radial magnetic fields [1]. To date, one of the primary propellants used for these devices was xenon (Xe) gas thanks to its high atomic mass and relatively low ionization energy (12.1 eV) among the inert gas species [5]. However, due to its scarcity, associated high production costs, and recent political influence, the price of Xe has risen [6, 7]. This is of concern for new space missions based on HETs and other electric propulsion technologies.

* Author to whom any correspondence should be addressed.



Original content from this work may be used under the terms of the [Creative Commons Attribution 4.0 licence](#). Any further distribution of this work must maintain attribution to the author(s) and the title of the work, journal citation and DOI.

For this reason, utilizing an alternative propellant for HETs is of great interest. Nevertheless, other cost-effective propellants must demonstrate acceptable performance in electric propulsion devices to justify a change in propellant choice. Many studies have thus investigated the performance and underlying physics for operation with various propellants such as iodine [8], krypton (Kr) [9–14], water vapor [15, 16], diatomic nitrogen (N_2), air [17, 18], and argon (Ar) [19, 20]. Among them, Kr (83.8 amu), which is the next heaviest noble gas to Xe (131.3 amu), is widely studied and reported to generally provide higher specific impulse due to the lighter mass at a low cost [13]. Similarly, Ar gas is also a promising propellant due to its even lower price than Kr. However, due to the lighter mass of Ar (39.9 amu) and higher ionization energy (15.2 eV) than other heavier inert gases, Ar exhibits lower ionization and thrust than that of other alternative propellants [19, 20].

Considering the recent increase in the number of HET-based mega-constellations that require an extensive amount of propellants [21], one possible avenue to reduce the total propellant cost and maintain performance is the utilization of a mixture of two different gas species at a proper ratio. In general, the utilization of a gas mixture has some propulsion system-level considerations. The gas mixture can be provided to the thruster by either a pre-mixed gas contained in one propellant tank or by two separate propellant tanks. The former would involve partial gas pressure calculations to assess propellant tank geometry, as well as a suitable propellant loading campaign in which the gas mixture would be generated. The latter would enable the injection of different mix ratios, thus throttling thruster operation. On the other hand, two separate tanks would take significantly more volume and require two separate propellant feeding systems. This might demand an additional enhancement in the thrust performances for the missions due to the increases in the mass and volume of the total system. Therefore, it is desirable first to investigate any possibility of enhancing performances by understanding underlying plasma physics, as it would help set up a system requirement quantitatively using multiple gas propellants. In particular, the optimal mixture of the noble gas may prevent a decrease in performance even with the use of a lighter propellant by leveraging the lower ionization energy and shorter ionization mean-free path of the heavier propellant.

Various mixtures of propellants have been used for HET operation. Kim *et al* operated an SPT-100 HET on a Xe–Kr gas mixture between a Kr mass fraction of 0%–100%, at 3–6 mg s⁻¹ total anode mass flow rate and discharge voltages of 200–650 V [22]. Kim argued that the thrust decreases due to the lower atomic mass of Kr. The study also showed that the thrust efficiency decreased approximately linearly with the increase in Kr mass fraction. Further analysis showed that the voltage efficiency and beam divergence remain approximately constant as more Kr was injected into the thruster, yet the mass utilization efficiency decreased. Ducci *et al* operated the Xe–Kr mixture HET at 2–7 kW for discharge voltages of 300–700 V [23]. At a fixed total anode flow rate and discharge voltage, the discharge current increased approximately linearly with the increase in Kr mass fraction. The study showed that the thrust and specific impulse both manifested an increase

by approximately 10%–20% at a fixed discharge voltage when raising the Kr mass fraction from 0%–100% while fixing the total flow rates of 8 mg s⁻¹ and 12 mg s⁻¹. The thrust efficiency was observed to decrease non-linearly with the increase in Kr mass fraction. Yamasaki *et al* modified the channel length of a 1-kW anode layer type HET and compared the performances of original and modified thrusters at different Xe–Ar mixture concentrations at a fixed total volumetric flow rate, 27.8 sccm [20]. For the modified HET, the specific impulse was enhanced significantly when compared to the original model at 0%–40% volumetric fractions of Xe, which exhibited the largest improvement from 482 s to 1500 s at the 0% Xe case. Gurciullo *et al* investigated the ion plume properties of a HET on Xe, Xe–N₂, and Xe-air mixtures at approximately 700 W of discharge power. In particular, the velocities, acceleration voltages, and current ratios of different Xe, O₂, and N₂ ion species were quantitatively separated at different fractions of mixtures by using an E×B probe [17].

Despite the above-described past studies on the gas-mixture HET plasmas, characterizing plasma parameters and analyzing the performance of the gas-mix-fed HET performances remains challenging. One of the main reasons is due to their different atomic properties, which makes it difficult to separate the quantitative contributions of different ion species to the thrust performance. In the case of Kr–Ar mixture plasmas, Kr has a mass approximately 2.1 times higher than that of Ar; thus, the doubly charged Kr ions might have a similar level of velocity with that of singly charged Ar ions, which makes the analysis relatively more complicated to separate their contributions to the total current and thrust. Moreover, the ionization region might vary with an increased Ar fraction in a Kr–Ar mixture due to the larger ionization mean free path in Ar compared with Kr inside the discharge channel. Therefore, the magnitude of the changes in the ionization region and their impact on the ion current of each species and thruster performance also requires thorough investigation to better understand the mixture-gas plasma, which is needed to use electric propulsion devices in space missions.

Therefore, we aim to understand the properties of Kr–Ar mixture HET plasmas, focusing on the extension of the ionization region and ion currents by each species, and quantify the enhancement in the performance by adding Ar to the pure Kr. We present the thruster performance at different Ar fractions using a 5 kW-class HET. Various plume ion diagnostics were utilized to analyze the ion currents made by each species and thrust performance. A correlation between generated ion densities and the ionization region is discussed in the Kr–Ar mixture plasma.

2. Experimental apparatus

In this study, a P5 5 kW-class HET and an EPL HCPEE 500 heater-type hollow cathode were used to investigate mixed Ar and Kr plasmas. The P5 was developed by the University of Michigan and Air Force Research Laboratory, which has been extensively studied both with Xe and Kr propellants [14, 24–26]. The test was conducted in Vacuum Test Facility 1

(VTF-1) at the Georgia Tech High-Power Electric Propulsion Laboratory. VTF-1 has a 4 m diameter and 7 m long length and is equipped with four NRC HS48-95 000 and two CVC PMC-32 C diffusion pumps along with two Leybold SV630B rotary vane pumps and two Leybold RA5001 roots pumps. Together, these provide a background pressure of approximately 10^{-6} Torr. In this study, the operating pressures were approximately 2.4×10^{-5} Torr-Kr and 3.1×10^{-5} Torr-Ar for both 79.7 sccm of Kr and 122.2 sccm of Ar, respectively, which are the high and low bounds for the test campaign. Even though the test conducted in this study includes Kr and Ar mixtures, the operational pressure lay between these bounds when using the partial pressures of each gas type. The pressure at the mixture gas was calculated by using an effective gas correction factor that was derived from a weighted summation of each correction factor γ_{eff} by the ratio of the mass flow rate of each injected gas across Ar fractions, i.e. $\gamma_{\text{eff}} = (\dot{m}_{\text{Kr}}\gamma_{\text{Kr}} + \dot{m}_{\text{Ar}}\gamma_{\text{Ar}}) / (\dot{m}_{\text{Kr}} + \dot{m}_{\text{Ar}})$, where \dot{m}_k and γ_k indicate the standardized volume flow rates in sccm and the gas correction factor of the species k , respectively.

Kr and Ar, both rated as ultra-high purity (99.999%), were used as propellants in the anode. Their mass flow rates were controlled by MKS GE50A mass flow controllers (MFCs) and their operational flow rates were verified with a MesaLabs DryCal 800 volumetric flowmeter. The uncertainties of the MFCs were 0.2% of the full scale or 1% of the setpoint depending on the flow rates, which led to the maximum ± 2 sccm for the anode, and ± 0.1 sccm for the cathode. Kr and Ar injected by each MFC were mixed in a cylindrical stainless-steel plenum located outside the vacuum chamber before reaching the anode. Pure Kr of 6.5 sccm was employed for an external cathode at all the setpoints in this study. It should be, therefore, noted that as the cathode flow rate remains constant throughout the entire test, the cathode flow fraction (CFF) varies with the total thruster flow rate. This was done for the ease of conducting the experiment without the need to use two mass flow controllers on the cathode line, each set at very low flow rates. This is also relevant for some flight propulsion systems, where a separate cathode-regulated flow module is used for a fixed cathode mass flow [27, 28]. Others in a similar manner are operated with a separately controlled cathode flow supply to constant the fraction of the anode-to-cathode flow rate [29, 30]. The CFF in this study changed in the range from 5.1% to 8.4% of the total anode flow rate. However, the effect of CFF changes in this range on the thruster operation is expected to be insignificant as the thrust, anode efficiency, voltage utilization efficiency, and cathode coupling voltage change less than 3% in the 5%–9% range of CFF as shown in [31]. The detailed diagrams of the vacuum chamber and propellant feed system are shown in figures 1(a) and (b). The discharge voltage of the thruster V_d was measured by a Fluke 83 V digital multimeter at the end of a discharge filter that provides approximately a 14 V decrease from the setpoint of the power supply. The discharge current I_d of the thruster was measured by a Tektronix CP030 current probe interlinked to a Tektronix HDO6104 oscilloscope.

An E×B probe was employed to measure the current fractions of each ion species, Kr^+ , Kr^{2+} , and Ar^+ , in the plume.

The probe is made up of a collimator with a diameter of 1.6 mm, and with a magnetic field of 0.16 T inside the probe body [32]. The voltage was scanned by a Keithley 2470 sourcemeter between the two plates to filter the velocity, and the collector current was acquired by a Keithley 6485 picoammeter. The rest position of the probe was located behind graphite shielding near the wall of the vacuum chamber to avoid long exposure to the ion beam and translationally moved by using two translational stages in order to acquire the dataset. The multiply charged ion current fractions were then measured at 1 m from the exit plane of the thruster.

In addition, a Faraday probe, a retarding potential analyzer (RPA), and a Langmuir probe were mounted on a rotating arm with a radius of 1 m to acquire angular profiles of the ion current density, axial ion energy distribution function (IEDF), and plasma potential. The rotation plane was aligned with the center of the thruster exit. The Keithley 2470 sourcemeter and Keithley 6485 picoammeter were used to scan the voltage and acquire the collector current for these probes. The raw ion current from the Faraday probe was corrected considering the secondary electron emissions induced by multiply-charged ions and the geometric effect following the method in reference [33]. The momentum-weighted beam angle, which describes axial momentum losses due to the divergence, was defined as $\theta_m = \cos^{-1}(I_{b,\text{ax}}/I_b)$, where $I_{b,\text{ax}}$ and I_b are shown as follows [33].

$$I_{b,\text{ax}} = \pi R^2 \int_{-\pi/2}^{\pi/2} j_b(\theta) \frac{k_D}{k_A} \cos(\alpha_N) \sin\theta d\theta, \quad (1)$$

$$I_b = \pi R^2 \int_{-\pi/2}^{\pi/2} j_b(\theta) \frac{k_D}{k_A} \sin\theta d\theta, \quad (2)$$

where R is the radius of the motor arm, θ is the half-angle with respect to the thruster axis, $j_b(\theta)$ is the measured angular profile of the ion beam current density. Parameters k_D , k_A , and α_N are correction factors that account for a thruster being deviated from a point source, and following the same definitions from reference [33]. The IEDF was measured by RPA at $\theta = 0$, and the voltage range was scanned within ranges of 0–350 V and 0–450 V with a resolution of 1 V for discharge voltages of 236 V and 386 V, respectively. The data were measured three times per each scan and smoothed by using the adjacent-averaging method. The cylindrical Langmuir probe with a tungsten tip length of 14.8 mm, and diameter of 0.1 mm was used to acquire plasma potential at 1 m from the thruster exit. The tip voltage was scanned three times at a range of 0–70 V. Finally, the thrust was measured by using a null-type inverted pendulum thrust stand [34].

3. Experimental results

The measured thrust and ion properties are presented across various Ar fractions. The Ar fraction described in this paper was defined as a ratio of standardized volumetric flow rates between Ar and the total Kr and Ar flow. We rather chose to

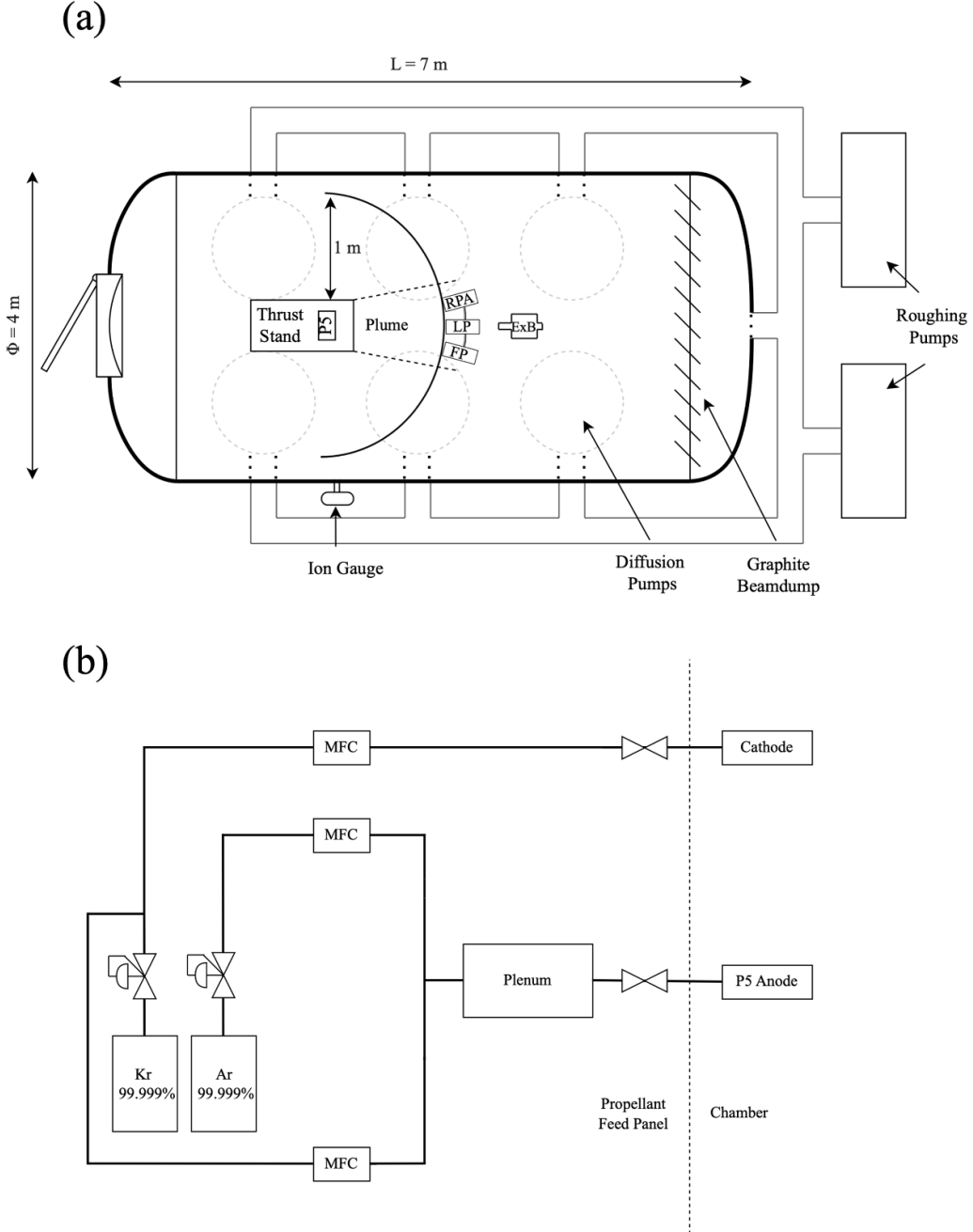


Figure 1. Schematic diagram of the (a) VTF-1 setup and (b) propellant feed system used in this study, where FP, RPA, LP and $E \times B$ refer to the Faraday probe, retarding potential analyzer, Langmuir probe, and $E \times B$ probe, respectively.

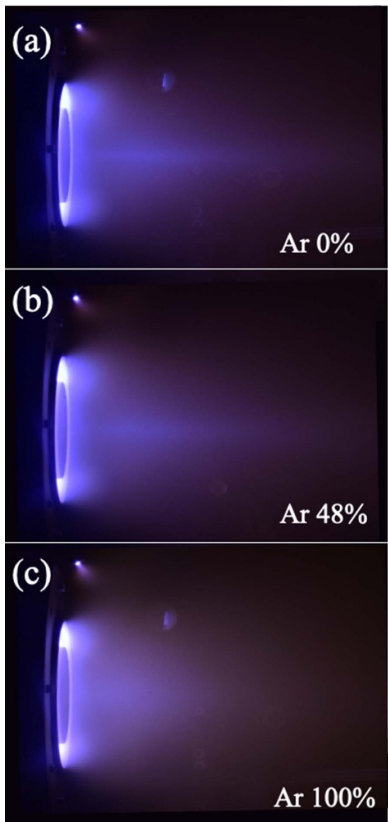
describe the standardized volumetric flow rates than mass in order to better relate the Ar fractions with the ion and neutral densities as discussed later. However, the mass flow rates of the operating conditions are also shown in table 1 which lists the detailed operating set points. The thruster was ignited with Kr, and the thruster body temperature was measured by a thermocouple. After the thruster reached a temperature greater than 200°C , a fraction of the Kr was replaced with Ar to reach each setpoint in table 1. This approach allowed the thruster to avoid the initially higher amplitudes of current oscillations when igniting at Kr–Ar mixtures. After reaching 200°C , the thruster operations exhibited a degree of oscillation, defined

as $\Delta I_d/I_d$, of approximately 18% to 31% at Kr–Ar mixtures, where ΔI_d is half of the discharge current peak-to-peak amplitude. The measurements were subsequently conducted. For future application-perspective research, the ignition process using the Kr–Ar mixture propellant has room to be further optimized in order to exhibit more stable initial discharges, particularly by arranging the operating sequences.

The thruster was operated at two discharge voltages of 236 V and 386 V which provide different maximum electron temperatures in the discharge channel [5]. However, the data-set of 80% and 100% Ar at 4.2 kW could not be acquired

Table 1. Operating conditions at different Ar fractions.

V_d (V)	I_d (A)	P_d (kW)	Kr sccm (mg s ⁻¹)	Ar sccm (mg s ⁻¹)	Volumetric (mass) Ar %	B-field (%)
236	10.8	2.6	77.7 (4.9)	0 (0)	0 (0)	100
236	10.8	2.6	64.7 (4.1)	22.3 (0.7)	26 (14)	100
236	10.9	2.6	49.1 (3.1)	45.8 (1.4)	48 (31)	100
236	10.7	2.5	23.7 (1.5)	88.4 (2.6)	79 (64)	100
236	11.2	2.7	0 (0)	126.7 (3.8)	100 (100)	100
386	10.6	4.1	79 (5.0)	0 (0)	0 (0)	200
386	10.8	4.2	61.9 (3.9)	22.3 (0.7)	26 (15)	200
386	10.9	4.2	46.3 (2.9)	44 (1.3)	49 (31)	200

**Figure 2.** Photographs of the Kr–Ar mixture plume plasmas at 236 V, (a) 0%, (b) 48%, and (c) 100% of Ar volumetric fractions.

in this study due to difficulties in maintaining the discharge using the identical magnetic fields with that of the 0%–48% Ar cases. Figure 2 shows an image of the P5 operating on a Kr–Ar mixture.

Statistical errors of volumetric flow rates and discharge currents in table 1, were derived from the standard deviation of three measurements under identical conditions during different thruster operations. The standard deviations of the flow rates and discharge currents were less than 3.3% and 1%, respectively, of the values presented in table 1. The only exception is the pure Ar case in which the standard deviation in discharge current of up to 10% was recorded. Despite lower statistical errors at the pure Ar when changing the magnetic

field, the field was kept constant over all the Ar concentrations to focus on the impact of the gas mixture on the plasma.

Figures 3(a)–(c) depict the thrust T , specific impulse I_{sp} , and anode efficiency η_a at different Ar concentrations for the two power levels. The specific impulse I_{sp} and anode efficiency η_a were defined as $I_{sp} = T/\dot{m}_a g$ and $\eta_a = T^2/2\dot{m}_a P_d$, respectively, where \dot{m}_a is the total anode mass flow rate, and P_d is the discharge power. The root sum of square method was used to calculate the total error [35]. The derived error bars in figures 3(a)–(c) include the statistical error of the measurement, which indicates the 95% confidence interval of three-times thrust measurement at each set point in table 1, and the inherent error of the thrust stand due to the thermal drift. The inherent error ratio of the thrust stand due to the thermal drift was less than 1.7% in this experiment.

The thrust gradually decreased as the Ar fraction rose because \dot{m}_a decreased as Ar gases were mixed even though the total volume flow rates were raised. However, the thrust did not decrease until after 26% Ar, and resulted in thrust of 76 mN and 78 mN at 0% and 26% Ar cases at 2.6 kW, respectively, even though the flow rate of Kr decreased from 77.7 sccm to 64.7 sccm. A similar trend was also observed at 4.1 kW, where 103 mN and 102 mN were found at the 0% and 26%-Ar cases, respectively. The difference between the total injected neutral densities of the two conditions, pure Kr and 26% of Ar, was estimated at approximately 5% when considering the mass flow rates in table 1. The ratio of injected total neutral number densities at different Ar concentrations was found from the relation between the mass flow rate and density, $n_k = \dot{m}_k / (M_k v_k A)$, where M is the atom mass, n is the number density, v is the thermal velocity, A is the area of the anode gap where the gas is injected, and the subscript k implies the gas species. Then, the ratio was derived as $n_{0\%Ar}/n_{26\%Ar} = (\dot{m}_{Kr}/\sqrt{M_{Kr}}) / (\dot{m}_{Kr}/\sqrt{M_{Kr}} + \dot{m}_{Ar}/\sqrt{M_{Ar}}) \sim 0.95$, where $n_{0\%Ar}$ and $n_{26\%Ar}$ are the injected neutral densities at the pure Kr and 26%-Ar cases, respectively.

As the total anode mass flow rate \dot{m}_a decreased along Ar fractions due to the lighter mass, the trend of the specific impulse deviates from that of thrust. At 2.6 kW, the specific impulse was approximately 6% higher in the 26%-Ar case than in the pure Kr case. However, the specific impulse of the pure Ar was 6% smaller than that of pure Kr even at their lighter mass probably due to the poor ionization or lower mass utilization due to the relatively low discharge voltage of 236 V, which

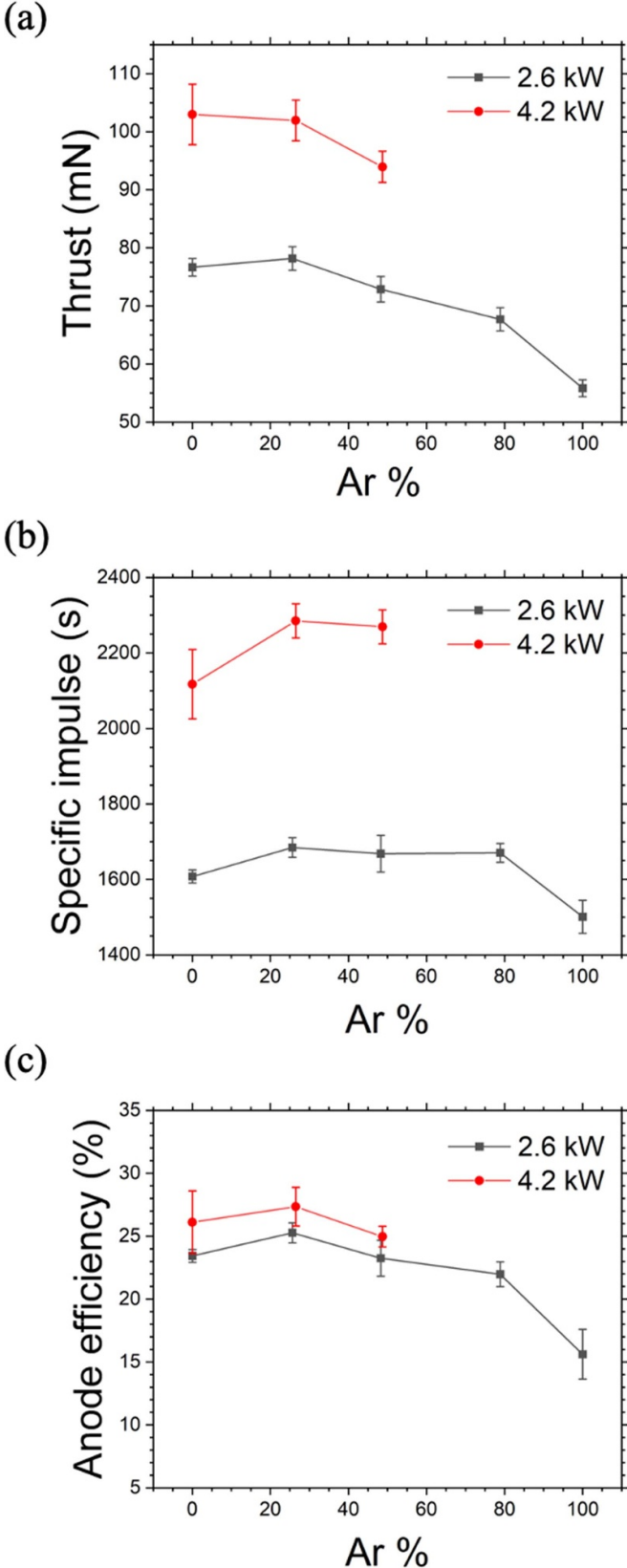


Figure 3. (a) Thrust (T), (b) specific impulse ($I_{sp} = T/\dot{m}_a g$), and (c) anode efficiency ($\eta_a = T^2/2\dot{m}_a P_d$) of the P5 at different Ar fractions. The black and red curves indicate two discharge voltage and power levels, 236 V at 2.6 kW and 386 V at 4.2 kW, respectively.

was also observed in Xe–Kr mixture plasmas [22]. The anode efficiency exhibited a similar trend with the thrust as shown in figure 3(c), where local maxima of 25% and 28% were found at 26%-Ar operation at 2.6 kW and 4.2 kW, respectively.

To analyze the performance in terms of ion properties, the current fractions of the mixture ion species and their contributions to the total ion current were first separated by using the $E \times B$ probe. Figure 4(a) shows the measured probe signals, where three representative data are shown at the 0%, 48%, and 100% Ar cases at 2.6 kW. As can be seen, the Kr^{2+} currents are overlapped with Ar^+ in the raw signals as they have similar most probable velocities. Therefore, the following analysis was conducted to fully separate each contribution of the ion species from the raw signals.

The most probable axial velocities of each species were derived from the $E \times B$ probe signals. In general, the velocity ratios of the ion species k are generally dependent on the atomic mass as $v_{i,k} \sim \sqrt{2q_k \Delta V_{b,k}/M_k}$, where q_k is the charge of the ion, $\Delta V_{b,k}$ is the acceleration voltage, and M_k is the atomic mass of the species k . By using the pure Kr (0% Ar case in figure 4(a)) trace, the ratio of two acceleration voltages of Kr^{2+} and Ar^+ ions, $\Delta V_{b,Kr^{2+}}/\Delta V_{b,Ar^+}$, was derived as 0.99. Similarly, when comparing the pure Kr with the pure Ar case, $\Delta V_{b,Ar^+}/\Delta V_{b,Kr^{2+}}$ was calculated as 0.97.

Therefore, the ratio of ion velocity between Ar^+ and Kr^{2+} can be calculated as follows

$$\frac{v_{i,Ar^+}}{v_{i,Kr^{2+}}} \sim \sqrt{\frac{\Delta V_{b,Ar^+} M_{Kr}}{2\Delta V_{b,Kr^{2+}} M_{Ar}}} \\ = \sqrt{\frac{1}{2} \left(\frac{M_{Kr}}{M_{Ar}} \right) \left(\frac{\Delta V_{b,Ar^+}}{\Delta V_{b,Kr^{2+}}} \right) \left(\frac{\Delta V_{b,Kr^{2+}}}{\Delta V_{b,Ar^+}} \right)} = 1.01. \quad (3)$$

This indicates a 1% difference in the most probable velocity of the Kr^{2+} and Ar^+ ions, which corresponds to approximately 0.5 V difference in the plate voltage of the $E \times B$ probe used in this study. For the above analysis, we assumed that the change of the ratio $\Delta V_{b,Kr^{2+}}/\Delta V_{b,Ar^+}$ across the Ar fractions is negligible. The peak velocity of Kr^+ from the $E \times B$ traces remained almost the same even at high Ar fractions, as also shown in figure 4(a). This suggests that $\Delta V_{b,Ar^+}$ did not change significantly across the Ar fractions; thus, we expect the same for the ratio $\Delta V_{b,Kr^{2+}}/\Delta V_{b,Ar^+}$ as most of Kr^{2+} ions are generated from the electron-impact ionization of Kr^+ [36].

Nearly identical most probable velocities of Kr^{2+} and Ar^+ ions suggested above imply that the cumulative trace of Ar^+ and Kr^{2+} currents in the $E \times B$ probe can be fitted by a single Gaussian with the same peak and then easily separated from each other once the amount of Kr^{2+} is known. However, there was no physical method to fully track the ratio between Kr^{2+} and Kr^+ currents, $I_{Kr^{2+}}/I_{Kr^+}$, at different Ar fractions. However, we expect that the current ratio $I_{Kr^{2+}}/I_{Kr^+}$ at the pure Kr case could be set as a low bound across the Ar fractions. In particular, the electron temperature should rise as the Ar fraction increases because the electrons are heated up

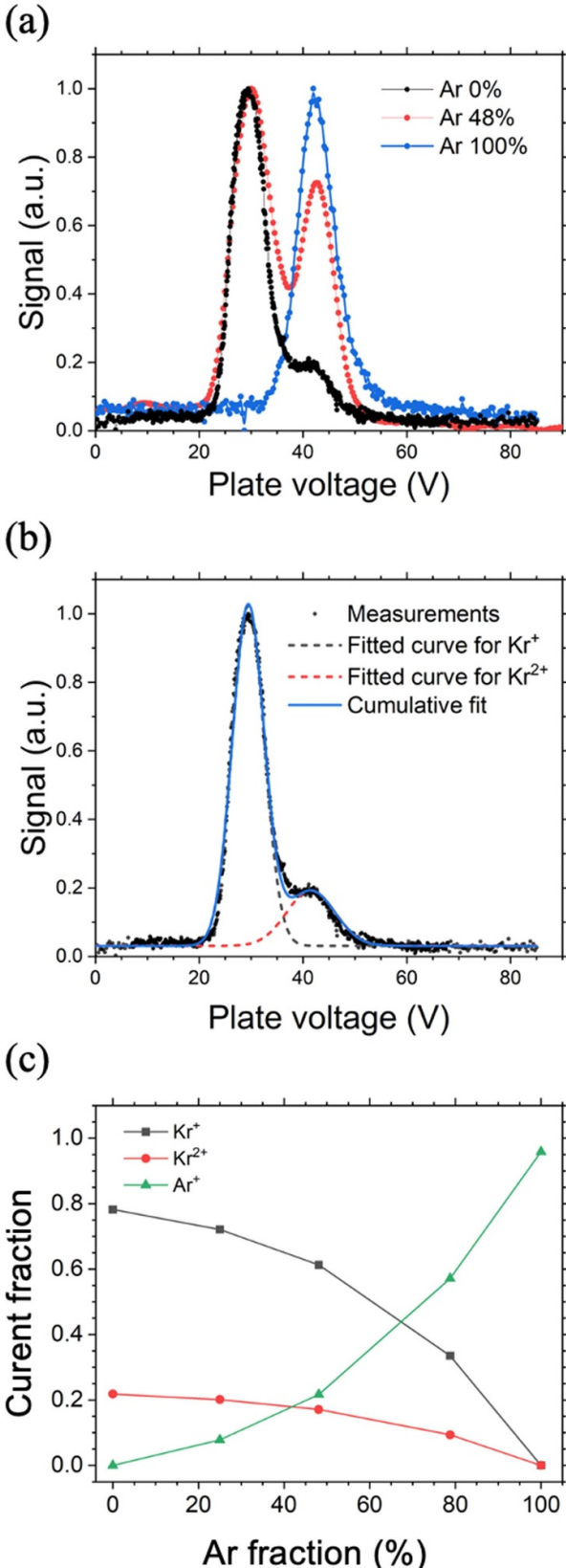


Figure 4. (a) Normalized E×B probe signals measured at different Ar fractions at 2.6 kW. (b) An example of the Gaussian-curve-fitted trace to separate ion currents from different species. (c) Normalized fractions of Kr⁺, Kr²⁺, and Ar⁺ current across Ar fractions.

to a higher level until they start losing the energy by ionizing Ar neutrals that have a higher ionization energy than that of Kr. This can also be inferred from a uniform discharge model assuming Maxwellian electron absorbing a constant power [37]. More directly, the probe experiment in Kr and Xe HET plasma presents higher electron temperatures in Kr than in Xe at the same discharge power [38, 39]. Moreover, an increased stepwise ionization of Kr⁺ at higher electron temperature will raise the ratio $I_{\text{Kr}^{2+}}/I_{\text{Kr}^+}$ [40]. For the conservative analysis, however, the low bound of $I_{\text{Kr}^{2+}}/I_{\text{Kr}^+}$ was used for all Ar fractions in this study based on the measurements of the pure Kr case. The fraction of Ar²⁺ ion current was neglected as the fraction was less than 5% in the case of pure Ar.

The current fractions of Kr⁺, Kr²⁺, and Ar⁺ were separated by fitting two Gaussian curves to the probe traces. The Ar⁺ currents at 26%–79% Ar cases were derived by subtracting the amount of Kr²⁺ currents using the low bound current ratio, $I_{\text{Kr}^{2+}}/I_{\text{Kr}^+}$. Figure 4(b) shows one representative fitting curve at pure Kr (0% Ar) case. The measured data were well-fitted with two Gaussians for all the cases with $R^2 > 0.99$. Figure 4(c) shows the consequent contributions of each ion species, where the contribution of Ar⁺ ion current to the total current is gradually increased across the Ar fractions while that of Kr⁺ and Kr²⁺ decreased.

Ion kinetic energies at different Ar fractions were investigated, and figure 5(a) depicts IEDFs derived at three representative Ar fractions. As a result, the full widths at half maximum were derived as shown in figure 5(b) with error bars that account for 95% confidence intervals of three-times measurement per each set point and inherent error. The width increased along the Ar fraction from 48 eV at 0% Ar to 78 eV at 100% Ar, which indicates an apparent trend of IEDF broadening.

Figure 6(a) shows the measured angular ion current distributions at different Ar concentrations. In order to correct the ions generated by charge-exchanged collisions, a low bound of the ion current distribution was used, which subtracted the current at the angle of 90° from the raw signals [11]. The corrected signals are shown as dotted lines in figure 6(a). As a result, the derived total ion beam current I_b and individual contributions of Kr and Ar ions are presented in figure 6(b). The error ratios in the measurements of the total ion beam current were less than 2%, and the contributions of Kr and Ar ions to the total beam current were derived using the current ratio between Kr⁺ and Kr²⁺ as previously mentioned. The contribution of the total Kr ion current, a summation of the two ion currents Kr⁺ and Kr²⁺, exhibited a local maximum at the 26%-Ar case as 4.4 A and then gradually decreased as the Ar fraction increased. In particular, the Kr ion current decreased less than the proportional decrease of Kr neutrals for low mixtures of Ar. The total Kr ion current at the 49%-Ar condition reduced only by 9% when compared to the 0% case even though the injected Kr neutral particles decreased by 37% which can be estimated from the ratio of the Kr flow rates. Then, 91% of the total Kr ion current dropped along 49%–100% Ar cases.

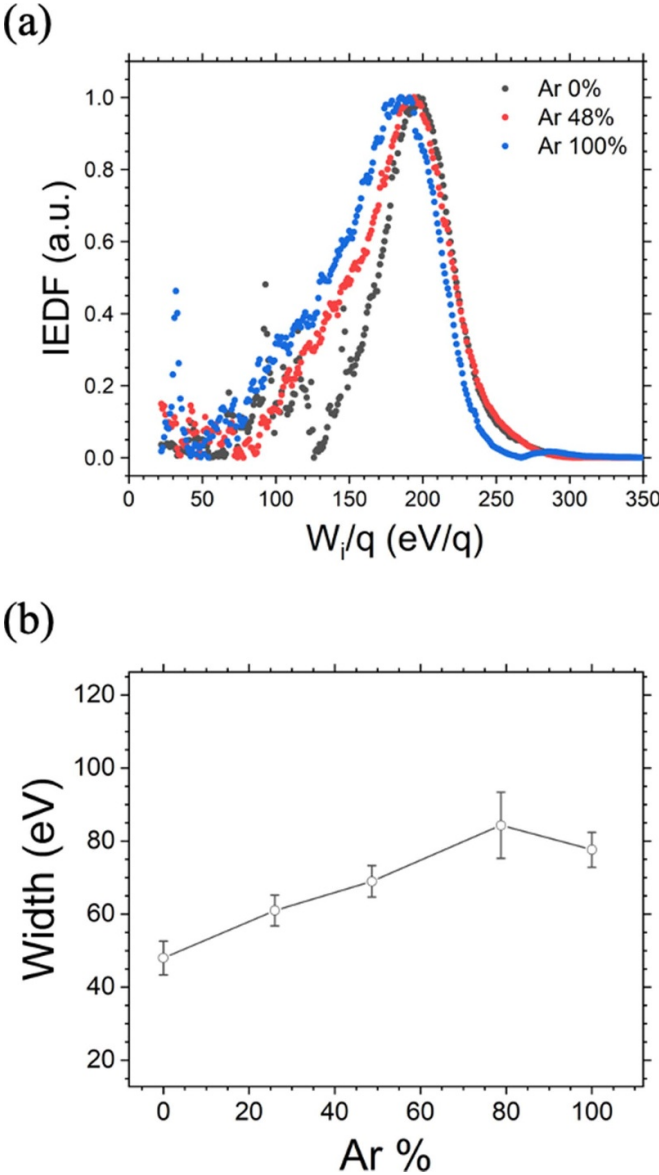


Figure 5. (a) IEDFs and their (b) full widths at half maximum at different Ar fractions at 2.6 kW.

On the other hand, the Ar^+ current increased along the Ar fractions and both of Ar and Kr ion currents contributed to enhancing the total ion beam current in all mixture cases.

Figure 6(c) represents the efficiency factors, where the current ($\eta_b = I_b/I_d$), mass ($\eta_m = (M_{\text{Kr}}I_{b,\text{Kr}}/em_a)\sum_k f_k/Z_k + M_{\text{Ar}}I_{b,\text{Ar}}/em_a$), voltage ($\eta_v = \Delta V_b/V_d$), and divergence utilization ($\eta_\theta = (\cos \theta_m)^2$) were calculated from each of the ion diagnostics described above. Here, f_k and Z_k are the normalized current fraction and the charge of the Kr ion species k , respectively, and ΔV_b is the acceleration voltage derived from the most probable ion kinetic energy in the IEDFs, ΔV_{mp} , subtracted by the local plasma potential ϕ_p , i.e. $\Delta V_b = \Delta V_{\text{mp}} - \phi_p$. As can be seen, the changes in the voltage and divergence utilization were not significant, where both were within a 10%

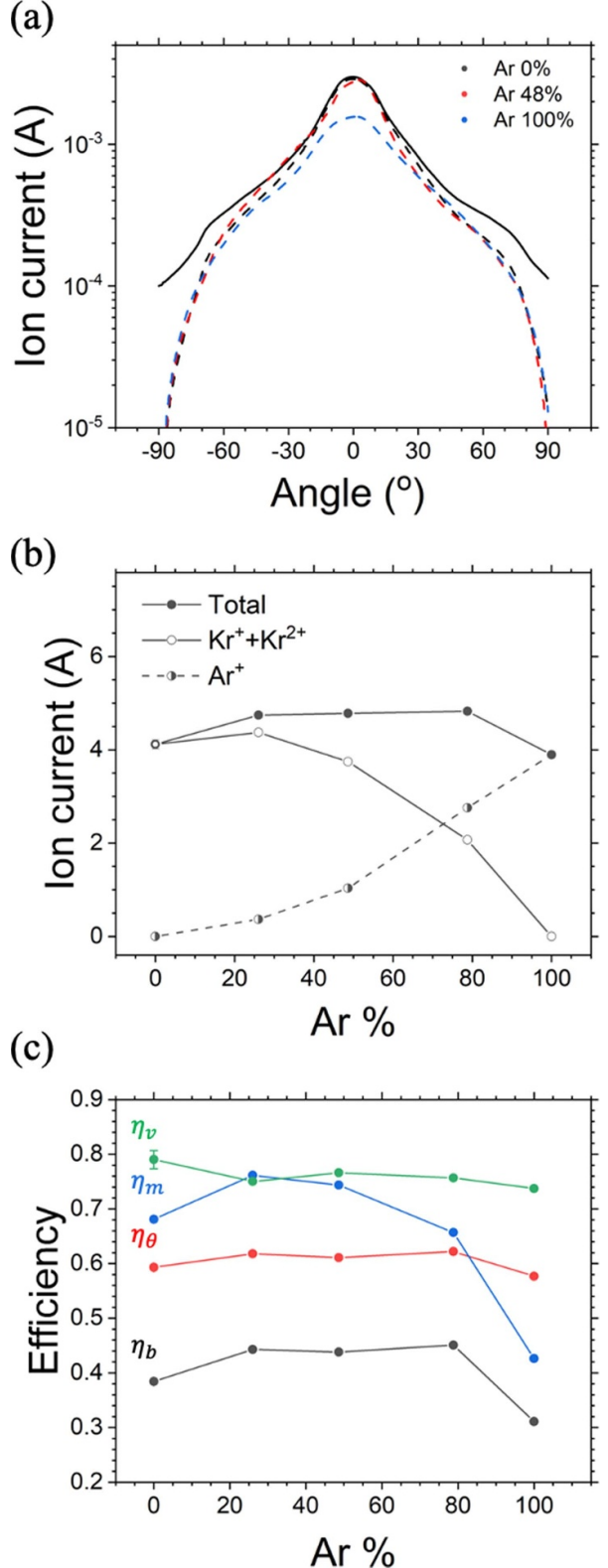


Figure 6. (a) Angular distribution of the ion current at 0% (black), 48% (red), and 100%-Ar (blue), where solid and dotted curves indicate raw and corrected signals, respectively, at 0%-Ar case. (b) Total and separated ion current fractions. (c) Calculated current ($\eta_b = I_b/I_d$), mass ($\eta_m = (M_{\text{Kr}}I_{b,\text{Kr}}/em_a)\sum_i f_i/Z_i + M_{\text{Ar}}I_{b,\text{Ar}}/em_a$), voltage ($\eta_v = \Delta V_{\text{mp}}/V_d$), and divergence utilization ($\eta_\theta = (\cos \theta_m)^2$). The dataset was measured at 2.6 kW.

difference across Ar fractions. Small changes up to 10% in the beam angle were also reported at SPT-100 Xe–Kr mixture plasmas at different mixture ratios [22].

Even though the 4.2 kW case, with a higher discharge voltage, was not fully investigated across the Ar concentrations, similar trends with those in 2.6 kW were found in the thrust performances and ion beam properties when compared to 0% and 26% Ar cases. The beam current slightly increased (5.0 A vs. 4.7 A) while an 18% increase in IEDF width at 20% of the maximum was found.

4. Discussion

We present detailed analyses of the ionization region and ion density at different Ar fractions based on the measurements and analytical models. We particularly focus on the cause of higher or similar levels of thrust at the 26%-Ar case when compared to the pure Kr even with the higher ionization energy and lighter mass of Ar when compared to Kr.

The width of the IEDF generally indicates the relative length of the ionization region overlapped with the acceleration region [41]. Therefore, an increased width of the IEDF as seen in figure 5(b) probably suggests an extension of the ionization region along the Ar fractions unless the acceleration region changes significantly. An increase in the low-energy part of IEDF indicates an increment of the fractions of the relatively slower ions with an extended ionization region mainly towards the downstream.

Moreover, changes in the length of the ionization region at the Kr–Ar mixture probably significantly impact the total ion current of both Ar and Kr. As we fixed the discharge voltage, the ion beam current of the ion species k , $I_{b,k}$, represents the ion number density $n_{i,k}$ generated inside the channel as $I_{b,k} = e n_{i,k} v_{i,k} A \propto n_{i,k}$, where A is the cross-sectional area of the discharge channel. To further understand the changes in the ionization region and the generated ion density across the Ar fraction, we attempted to derive an analytical form of the characteristic length of ionization and the Kr ion densities in the Kr–Ar mixture plasmas in the following sections.

For the analysis, any arbitrary physical parameter f was assumed as $f = f_0 + \tilde{f}(t)$, where f_0 is a quantity at the equilibrium, and $\tilde{f}(t) \sim f_0 e^{-i\omega t}$ is the perturbation solution with an oscillation frequency ω . Therefore, averaging parameters over the oscillation period further simplifies the equation using $\bar{f} = f_0$, where the superscript \bar{f} indicates a time-averaged parameter. We assumed both Ar and Kr are injected into the ionization region ($n_{\text{Kr}} > 0$ and $n_{\text{Ar}} > 0$), and used the continuity equation for ion species k as follows.

$$\overline{\frac{\partial n_{i,k}}{\partial t}} + \nabla \cdot \overline{(n_{i,k} v_{i,k})} \cong \frac{\bar{n}_{i,k} \bar{v}_{i,k}}{L} = \dot{n}_{i,k}, \quad (4)$$

where L is the characteristic length of the ionization. The above assumptions and the time-averaged equation consequently lead equations (4) and (5).

$$\bar{n}_{i,k} \cong \bar{n}_e \bar{n}_{n,k} \frac{\langle \sigma_{i,k} v_e \rangle L}{\bar{v}_{i,k}}, \quad (5)$$

when using $\dot{n}_{i,k} = n_{n,k} n_e \langle \sigma_{i,k} v_e \rangle$. Here, n_e is the electron density, $v_{i,k}$ is the ion velocity, $n_{n,k}$ is the neutral density, $\sigma_{i,k}$ is the ionization cross section. The subscript k indicates the parameter of either Kr or Ar. Then the ion density of each species can be written as follows in equations (6) and (7) assuming quasi-neutrality and singly charged ions, $n_e \approx \sum_k n_{i,k}$ for the simplicity.

$$\bar{n}_{i,Kr} = \frac{\bar{n}_{n,Kr} \bar{n}_{i,Kr} K_{Kr}(T_e) L}{\bar{v}_{i,Kr}} \left(\frac{1}{1 - \bar{n}_{n,Kr} K_{Kr}(T_e) L / \bar{v}_{i,Kr}} \right), \quad (6)$$

$$\bar{n}_{i,Ar} = \frac{\bar{n}_{n,Ar} \bar{n}_{i,Ar} K_{Ar}(T_e) L}{\bar{v}_{i,Ar}} \left(\frac{1}{1 - \bar{n}_{n,Ar} K_{Ar}(T_e) L / \bar{v}_{i,Ar}} \right) \quad (7)$$

$$L = \frac{\bar{v}_{i,Ar} \bar{v}_{i,Kr} / (\bar{n}_{n,Kr} + \bar{n}_{n,Ar})}{\bar{v}_{i,Ar} K_{Kr}(T_e) - b_{Ar} (\bar{v}_{i,Ar} K_{Kr}(T_e) - \bar{v}_{i,Kr} K_{Ar}(T_e))}, \quad (8)$$

where e is the electron charge, $K_{Kr}(T_e)$ is the ionization rate coefficient of the Kr neutrals averaged over the Maxwellian electron energy distribution, i.e. $K_{Kr}(T_e) = \langle \sigma_{i,Kr} v_e \rangle$, and b_{Ar} is the fraction of the Ar neutral density defined as $b_{Ar} = \bar{n}_{n,Ar} / (\bar{n}_{n,Kr} + \bar{n}_{n,Ar})$. The characteristic length of ionization L was algebraically derived by combining the Kr^+ and Ar^+ ion densities from equations (6) and (7), i.e. the Ar^+ ion density at equation (6) is replaced by the derived Ar^+ ion density from equation (7), which provides the analytic form of L as shown in equation (8). When considering $\bar{v}_{i,Ar} K_{Kr}(T_e) > \bar{v}_{i,Kr} K_{Ar}(T_e)$ due to the lighter mass of Ar and higher ionization cross section of Kr [42], equation (7) suggests the ionization region is gradually extended across the Ar fractions as inferred from the RPA data.

For pure Kr and Ar (0% and 100% Ar) cases, where equations (6) and (7) cannot be used due to the absence of the admixture, the continuity equation for pure ion species k was used to calculate L . This provides $L = \bar{v}_{i,k} / \bar{n}_{n,k} K_k(T_e)$ from equation (4) and assuming $\bar{n}_e \approx \bar{n}_{i,k}$. Moreover, the pure ion density $\bar{n}_{i,k}$ was calculated from the continuity equation of the neutral particle as shown in equation (9), which results in $\bar{n}_{i,k} = \bar{n}_{n,k} / K_k(T_e) L$ when using $\bar{n}_e \approx \bar{n}_{i,k}$.

$$\nabla \cdot \overline{(n_{n,k} v_{n,k})} \cong \bar{n}_{n,k} \bar{v}_{n,k} / L = \bar{n}_{n,k} \bar{n}_e K_k(T_e). \quad (9)$$

We calculated the Kr ion density and characteristic length to understand their qualitative trends and quantitatively figure out the validity of the model based on equations (6)–(8). We used the time-averaged diagnostics results previously described. To calculate the Kr ion density from equation (6), we assumed the electron temperature of 20 eV, which is approximately one-tenth of the applied discharge voltage [5]. Even though we assumed electron temperature, the dependency of the final density on the temperature was negligible as will be discussed later. Then, the measured acceleration voltage (figure 6(c)) was used to calculate the ion velocity, $v_{i,Kr} \sim \sqrt{2\Delta V_b/M_{Kr}}$ with singly charged Kr and Ar ions. The neutral density was

calculated from $n_{n,\text{Kr}} = \dot{m}_{\text{Kr}} / (M_{\text{Kr}} v_{n,\text{Kr}} A)$, and the ion current by the injected Ar admixture, $\bar{n}_{i,\text{Ar}}$ in equation (6) was derived from the Ar^+ component from the total ion current, $\bar{n}_{i,\text{Ar}} = \bar{I}_{b,\text{Ar}} / e \bar{v}_{i,\text{Ar}} A$ (figure 6(b)). M_{Kr} and $v_{n,\text{Kr}}$ indicate the mass and thermal velocity of Kr, respectively. The rate coefficient $K_{\text{Kr}}(T_e)$ was calculated by averaging over a Maxwellian velocity distribution using the electron-impact ionization cross sections [42]. The Ar^+ ion density in equation (7) was derived by using the same way as conducted for the Kr^+ ion. The calculated ion densities are compared with the densities directly derived from the measured ion current of each species (figure 6(b)), from $\bar{n}_{i,k} = \bar{I}_{b,k} / e \bar{v}_{i,k} A$, where $\bar{I}_{b,k}$ indicates the either Kr^+ or Ar^+ ion current.

Figure 7(a) shows the calculated model using equation (6), where a good agreement with the direct measurement is found for both neutral gases. Larger discrepancies at the pure Kr and Ar cases are considered to be due to using an assumption for the continuity equations of neutral particles where all of the injected neutrals are ionized within the length L . As found in the low mass utilization towards the pure Kr in figure 6(c), the neutrals are generally not fully ionized and may have impacts on the results. Even though we assumed the electron temperature as 20 eV, the calculated ion densities exhibited similar values within 5% at a range of 15–25 eV due to little variation of the term $K_{\text{Kr}}(T_e)L$ along the electron temperature.

To estimate the characteristic length, L , we assumed a gas temperature of 950 K from the [43]. Figure 7(b) depicts the calculated length extended as the Ar fraction increased from approximately 6.1 mm to 11.8 mm. The derived L in this study indicates a length within which all the neutral particles are ionized inside the channel, and can indirectly be compared with spatial widths of the ionization frequency profiles inside the channel. At a kW-class HET, the ionization frequency was derived from the measured ion velocity distribution functions by LIF, and the width of the ionization frequency manifests an order of 10 mm inside the channel [44]. More directly, recent numerical analysis using Hall2De on a 6 kW Hall thruster H6US showed that the neutral Kr particles decrease by an order from $5 \times 10^{19} \text{ m}^{-3}$ to $5 \times 10^{18} \text{ m}^{-3}$ within an approximate length of 20% of the channel length [36]. This corresponds to 7.6 mm for the thruster used in this study and lies within the same order as 6.2 mm calculated at the pure Kr case as shown in figure 7(b).

Unlike the density in figure 7(a), the calculated length L depends both on the electron and gas temperature; however, the trend of increasing L at a higher Ar fraction was apparent. Moreover, the characteristic length also depends on the estimated neutral density at the inlet of the ionization region, which is vulnerable to errors as we estimated by using a simplified relation, $n_{n,\text{Kr}} = \dot{m}_{\text{Kr}} / (M_{\text{Kr}} v_{n,\text{Kr}} A)$, as previously described. Thus, even though the calculated increment of L from 0% to 26% Ar fraction is small, we believe this would be larger in reality as can be inferred from a significant broadening of the IEDF measurements shown in figure 5(b). Further in-detail analysis will be needed in the future.

Similarly to the current analysis, the estimated Kr^+ ion density also exhibited a local maximum at the 26%-Ar case

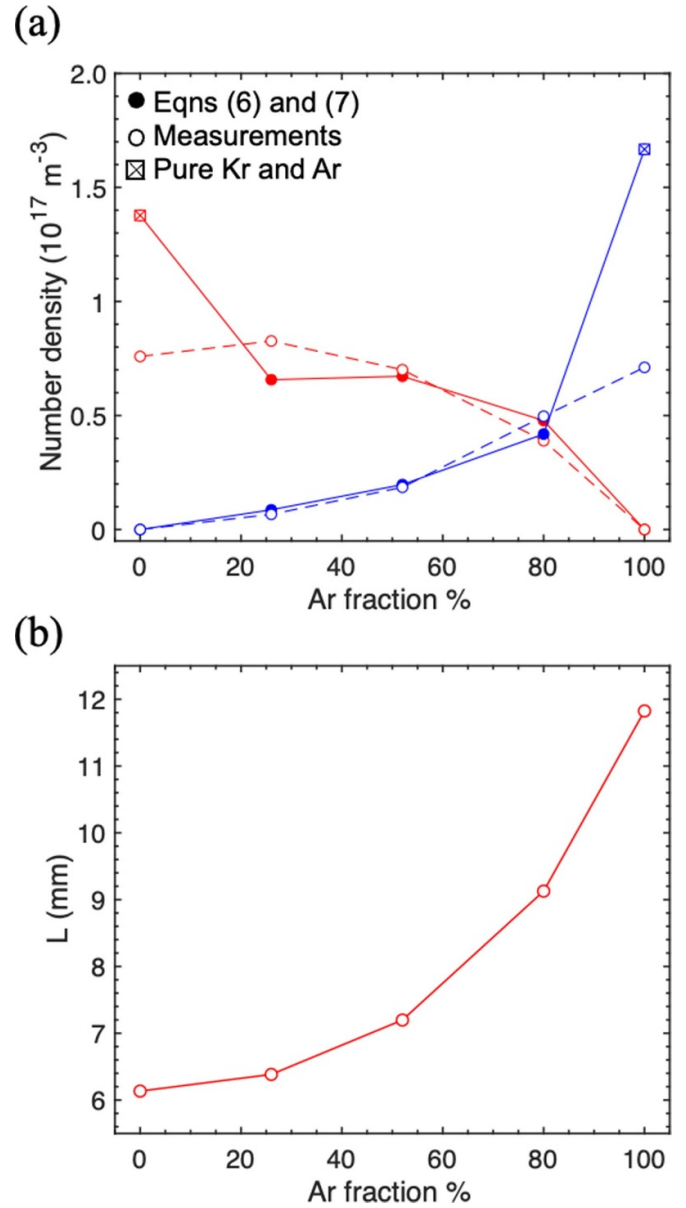


Figure 7. (a) Comparison of the ion densities derived from the model and measurements. (filled circle: calculated densities using Equations (6) and (7), empty circle: densities from the measurements, square: densities at pure Kr and Ar) (b) Calculated ionization length L from equation 8.

and a small decrease of less than 9% at the 48% case when compared to the pure Kr case, respectively. The Kr neutral density $n_{n,\text{Kr}}$ reduced as much as 16% and 39%, respectively at 26% and 48% Ar cases. This suggests that the ionization of injected Kr neutrals was enhanced when some Kr was replaced with Ar.

It is considered that the ionization of Kr is enhanced in the mixture plasmas due to an extended L and the presence of high-temperature seed electrons that are provided by the ionized Ar. In particular, the residence time of Kr was increased by extending the ionization region when Ar neutrals were injected. Due to the increased mean-free path, Ar

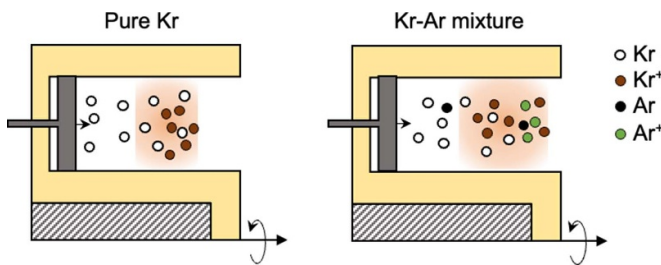


Figure 8. Schematic diagram for an extended ionization of Kr–Ar mixture inside the discharge channel.

neutrals are more likely to be ionized by a distribution of electrons located further downstream toward the exit plane, and typical magnetic-field strength downstream is still strong enough to confine the generated electrons. This is because, in Hall thrusters, the ionization region is relatively located upstream while overlapping with the acceleration region [5], and the spatial distribution of the acceleration region corresponds to the magnetic field profile, i.e. $E \propto j_D B^2 / (m_e \nu_{ef} n_e)$ [45]. In this relation, E is the electric field, j_D is the discharge current density, m_e is the electron mass, n_e is the electron density, and ν_{ef} is the effective collision frequency. Therefore, the strength of the magnetic field generally increases towards the exit plane and is sufficiently strong to confine the local electrons in downstream of the extended ionization region. The energetic electrons in the edge of the extended ionization region then contributes to the ionization of Kr neutrals with an ionization rate $\dot{n} = n_n n_e \langle \sigma_i v_e \rangle$. Consequently, this led Kr neutrals to pass through an extended ionization region with a longer residence time upon injecting Ar, which increases the ionization of Kr and the total Kr ion current as shown in figure 6(b).

As the Ar fraction increased, $n_{n,\text{Kr}}$ decreased towards the zero and this eventually reduced $n_{i,\text{Kr}}$ even though the ionization length L was largely extended according to equation (6). Therefore, the decrease in $n_{i,\text{Kr}}$ could be much less than the relative decrease in $n_{n,\text{Kr}}$ until a certain Ar fraction, which was 0%–48% in this case. We depicted schematics describing the ionization regions in both pure Kr and mixture cases in figure 8.

The enhanced ionization of Kr is considered the main cause of the higher or comparable thrust at 26% Ar than that of the 0% Ar case shown in figure 3(a). As the thrust generated by ion species k can be derived from the measured ion properties, $T_k = \dot{m}_{i,k} v_{i,k} = I_{b,k} \sqrt{M_k \Delta V_{b,k} / e} \cos(\theta_m)$ [5, 46], the thrust by Kr ions did not decrease at the 26% case when compared to the 0% case mainly due to the higher Kr ion current as described previously. The changes in the other efficiency parameters such as the beam angle and acceleration voltage were negligible between those two set points as shown in figure 6(c). The results, therefore, indicate that replacing a small portion of Kr to Ar provides as efficient performances as the pure Kr does at the same power level even at the higher ionization energy and lighter mass of Ar than those of Kr. The improved ionization of the main propellant Kr due to a longer residence time in the extended the ionization region and generated Ar⁺ current itself are the causes.

5. Conclusion

In this study, the effect of Ar gas admixture on a 5 kW HET operation on Kr is investigated in terms of thrust performances and ion properties. Even though its higher ionization energy and lighter mass, injecting a small fraction of Ar enhanced the ionization of Kr at the constant discharge power by extending the ionization region, which led Kr neutrals to spend a longer residence time, and by providing the energetic seed electrons. This eventually led to a similar thrust performance at the 26% Ar mixture when compared to the pure Kr. The study implies that mixing Ar approximately 26% volumetrically or 14% in the mass of the total propellants can be beneficial for the missions in that the same or even better thrust performance parameters are achieved at the same discharge power with lower total cost for the propellant. The advantage will particularly be notable at missions that require high total impulses such as deep space or mega-constellation missions.

Data availability statement

The data cannot be made publicly available upon publication because no suitable repository exists for hosting data in this field of study. The data that support the findings of this study are available upon reasonable request from the authors.

Acknowledgments

The authors thank Luke A Marino and Chhavi for their assistance in acquiring the experimental data for this study.

ORCID iDs

- Dongho Lee  <https://orcid.org/0000-0002-7231-9008>
Dan Lev  <https://orcid.org/0000-0001-7471-3909>
Mitchell L R Walker  <https://orcid.org/0000-0001-8829-0062>

References

- [1] Boeuf J P 2017 Tutorial: physics and modeling of Hall thrusters *J. Appl. Phys.* **121** 011101
- [2] Mazouffre S 2016 Electric propulsion for satellites and spacecraft: established technologies and novel approaches *Plasma Sources Sci. Technol.* **25** 033002
- [3] Lev D, Myers R M, Lemmer K M, Kolbeck J, Koizumi H and Polzin K 2019 The technological and commercial expansion of electric propulsion *Acta Astronaut.* **159** 213–27
- [4] Lev D, Myers R M, Lemmer K M, Kolbeck J, Koizumi H and Polzin K 2017 The technological and commercial expansion of electric propulsion in the past 24 Years *35th Int. Electr. Propuls. Conf. (Atlanta, GA)* (IEPC) p 242
- [5] Goebel D M and Katz I 2008 *Fundamentals of Electric Propulsion: Ion and Hall Thrusters* (Wiley)
- [6] Fazio N, Gabriel S B, Golosnoy I O and Wollenhaupt B 2019 Mission cost for gridded ion engines using alternative propellants *36th Int. Electr. Propuls. Conf. (Vienna, Austria)* (IEPC) p 831

- [7] The Economist, How rare-gas supply adapted to Russia's war (available at: www.economist.com/finance-and-economics/2023/03/30/how-rare-gas-supply-adapted-to-russias-war) (Accessed 1 September 2023)
- [8] Szabo J, Tedrake R, Metivier E, Paintal S and Taillefer Z 2017 Characterization of a one hundred watt, long lifetime Hall effect thruster for small spacecraft 53rd AIAA/ASME/ASEE Jt. Propuls. Conf. (Atlanta, GA) (AIAA) p 4728
- [9] Zhang G, Ren J, Tang H, Wang Y, Zhang Z, Liu J, Pan R, Zhang Z and Cao J 2023 Plasma diagnosis inside the discharge channel of a low-power Hall thruster working on Xe/Kr mixtures *Acta Astronaut.* **204** 389–401
- [10] Kim Y, Lee D, Doh G and Park J 2022 Performance comparison of xenon and krypton discharges in a 300 W-class Hall thruster, 37th Int. Electr. Propuls. Conf. (Boston, MA) (IEPC) p 336
- [11] Su L L, Marks T A and Jorns B A 2022 Investigation into the efficiency gap between krypton and xenon operation on a magnetically shielded Hall thruster 37th Int. Electr. Propuls. Conf. (Boston, MA) (IEPC) p 366
- [12] Linnell J and Gallimore A 2006 Internal Langmuir probe mapping of a Hall thruster with xenon and krypton propellant 42nd AIAA/ASME/SAE/ASEE Jt. Propuls. Conf. Exhib. (Sacramento, CA) (AIAA) p 4470
- [13] Su L L and Jorns B A 2021 Performance comparison of a 9-kW magnetically shielded Hall thruster operating on xenon and krypton *J. Appl. Phys.* **130** 163306
- [14] Linnell J A and Gallimore A D 2006 Internal plasma potential measurements of a Hall thruster using plasma lens focusing *Phys. Plasmas* **13** 103504
- [15] Schwertheim A and Knoll A 2021 Low power thrust measurements of the water electrolysis Hall effect thruster *CEAS Space J.* **14** 3–17
- [16] Tejeda J M and Knoll A 2023 A water vapour fuelled Hall effect thruster: characterization and comparison with oxygen *Acta Astronaut.* **211** 702–15
- [17] Gurciullo A, Fabris A L and Cappelli M A 2019 Ion plume investigation of a Hall effect thruster operating with Xe/N₂ and Xe/air mixtures *J. Phys. D: Appl. Phys.* **52** 464003
- [18] Marchionni F and Cappelli M A 2021 Extended channel Hall thruster for air-breathing electric propulsion *J. Appl. Phys.* **130** 053306
- [19] Yamasaki J, Yokota S and Shimamura K 2019 Performance enhancement of an argon-based propellant in a Hall thruster *Vacuum* **167** 520–3
- [20] Yamasaki J, Yokota S and Shimamura K 2017 Performance enhancement of anode-layer-type Hall thruster using mixture propellant 35th Int. Electr. Propuls. Conf. (Atlanta, GA) (IEPC) p 345
- [21] Potrivitu G C, Sun Y, Bin Rohaizat M W A, Cherkun O, Xu L, Huang S and Xu S 2020 A review of low-power electric propulsion research at the space propulsion centre Singapore *Aerospace* **7** 67
- [22] Kim V, Popov G, Kozlov V, Skrylnikov A and Grdlichko D 2001 Investigation of SPT performance and particularities of its operation with Kr and Kr/Xe Mixtures 27th Int. Electr. Propuls. Conf. (Pasadena, CA) (IEPC) p 065
- [23] Ducci C, Andreussi T, Arkhipov A, Passaro A, Andrenucci M, Bulit A and Edwards C 2015 Investigation of a 5 kW class Hall-effect thruster operating with different xenon-krypton mixtures 34th Int. Electr. Propuls. Conf. (Hyogo-Kobe, Japan) (IEPC) p 126
- [24] Gallimore A D 2003 What We have learned by studying the P5 Hall thruster *AIP Conf. Proc.* **533** 533–40
- [25] Haas J and Gallimore A 2000 An investigation of internal ion number density and electron temperature profiles in a laboratory-model Hall thruster 36th AIAA/ASME/SAE/ASEE Jt. Propuls. Conf. (Huntsville, AL) (AIAA) p 3422
- [26] Gulczinski F S III, Hofer R R and Gallimore A D 1999 Near-field ion energy and species measurements of a 5 kW laboratory Hall thruster 35th AIAA/ASME/SAE/ASEE Jt. Propuls. Conf. Exhib. (Los Angeles, CA) (AIAA) p 2430
- [27] Herscovitz J et al 2017 VENμS—A novel technological mission using electric propulsion 35th Int. Electr. Propuls. Conf. (Atlanta, GA) (IEPC) p 213
- [28] Sommerville J D, Fruncek C E, King L B, Makela J M, Terhune K J, Washeleski R L and Myers R M 2019 Performance of the Aurora low-power hall-effect thruster 36th Int. Electr. Propuls. Conf. (Vienna, Austria) (IEPC) p 740
- [29] Xu S, Welander B, Corey R, Leslie M, Bourguignon E and Fraselle S 2017 Testing of the PPU Mk₃ with the XR—5 Hall effect thruster 35th Int. Electr. Propuls. Conf. (Atlanta, GA) (IEPC) p 199
- [30] Jackson J, Cassady J, Allen M, Myers R, Tofil T, Herman D and Pencil E 2018 Development of high power hall thruster systems to enable the NASA exploration vision, *Sp. Propuls. 2018* (Seville, Spain) pp SP2018-00429
- [31] Goebel D M, Jameson K K and Hofer R R 2012 Hall thruster cathode flow impact on coupling voltage and cathode life *J. Propul. Power* **28** 355–63
- [32] Hofer R R, Haas J M and Gallimore A D 2003 Ion voltage diagnostics in the far-field plume of a high-specific impulse Hall thruster 39th AIAA/ASME/SAE/ASEE Jt. Propuls. Conf. Exhib. (Reno, NV) (AIAA) p 4556
- [33] Brown D L 2017 Recommended practice for use of Faraday probes in electric propulsion testing *J. Propul. Power* **33** 614–37
- [34] Xu K G and Walker M L R 2009 High-power, null-type, inverted pendulum thrust stand *Rev. Sci. Instrum.* **80** 055103
- [35] Mackey J, Haag T, Kamhawi H, Hall S and Peterson P 2018 Uncertainty in inverted pendulum thrust measurements *AIAA Propuls. Energy Forum* (Cincinnati, Ohio) (AIAA) p 4516
- [36] Dragnea H C, Lopez Ortega A, Kamhawi H and Boyd I D 2020 Simulation of a hall effect thruster using krypton propellant *J. Propul. Power* **36** 335–45
- [37] Liberman M A and Lichtenberg A J 2005 *Principles of Plasma Discharges and Materials Processing* (Wiley)
- [38] Linnell J A and Gallimore A D 2006 Internal plasma potential measurements of a Hall thruster using xenon and krypton propellant *Phys. Plasmas* **13** 093502
- [39] Linnell J A and Gallimore A D 2005 Internal plasma structure measurements of a Hall thruster using xenon and krypton propellant 29th Int. Electr. Propuls. Conf. (Princeton, NJ) (IEPC) p 024
- [40] Kim H, Lim Y, Choe W and Seon J 2014 Effect of multiply charged ions on the performance and beam characteristics in annular and cylindrical type Hall thruster plasmas *Appl. Phys. Lett.* **105** 144104
- [41] Reid B M 2009 The influence of neutral flow rate in the operation of Hall thrusters *PhD Thesis* University of Michigan (<https://doi.org/10.1063/1.3152218>)
- [42] Biagi S F database (MAGBOLTZ version 8.97) (available at: www.lxcat.net) (Accessed 21 August 2023)
- [43] Book C F and Walker M L R 2010 Effect of anode temperature on hall thruster performance *J. Propul. Power* **26** 1036–44
- [44] Pérez-Luna J, Hagelaar G J M, Garrigues L and Boeuf J P 2009 Method to obtain the electric field and the ionization frequency from laser induced fluorescence measurements *Plasma Sources Sci. Technol.* **18** 034008
- [45] Sekerak M J, Longmier B W, Gallimore A D, Brown D L, Hofer R R and Polk J E 2015 Azimuthal spoke propagation in hall effect thrusters *IEEE Trans. Plasma Sci.* **43** 72–85
- [46] Conversano R W, Goebel D M, Mikellides I G, Hofer R R, Wirz R E, Mikellides I G and Wirz R E 2017 Performance analysis of a low-power magnetically shielded Hall thruster: experiments *J. Propul. Power* **33** 975–83